NASA Technical Memorandum 101074

Aerodynamic Interaction Between Vortical Wakes and Lifting Two-Dimensional Bodies

Paul M. Stremel

(NASA-TM-101074) AERODYNAMIC INTERACTION BETWEEN VORTICAL WAKES AND LIFTING TWO-DIMENSIONAL BODIES (NASA. Ames Research Center) 34 p
CSCL 20D
N89-24563
Unclas
G3/34 0205449

March 1989

National Aeronautics and
Space Administration

NASA Technical Memorandum 101074

Aerodynamic Interaction Between Vortical Wakes and Lifting Two-Dimensional Bodies

Paul M. Stremel, Ames Research Center, Moffett Field, California

March 1989

National Aeronautics and
Space Administration

Ames Research Center
Moffett Field, California 94035

SUMMARY

Unsteady rotor wake interactions with the empennage, tail boom, and other aerodynamic surfaces of a helicopter have a significant influence on its aerodynamic performance, the ride quality, and vibration. A numerical method for computing the aerodynamic interaction between an interacting vortex wake and the viscous flow about arbitrary two-dimensional bodies has been developed to address this helicopter problem. The method solves for the flow field velocities on a body-fitted computational mesh using finite-difference techniques. The interacting vortex wake is represented by an array of discrete vortices which, in turn, are represented by a finite-core model. The evolution of the interacting vortex wake is calculated by Lagrangian techniques. The viscous flow field of the two-dimensional body is calculated on an Eulerian grid. The flow around circular and elliptic cylinders in the absence of an interacting vortex wake has been calculated. These results compare very well with other numerical results and with results obtained from experiment and thereby demonstrate the accuracy of the viscous solution. The interaction of a rotor wake with the flow about a 4:1 elliptic cylinder at 45° incidence was calculated for a Reynolds number of 3000. The results demonstrate the significant variations in the lift and drag on the elliptic cylinder in the presence of the interacting rotor wake.

SYMBOLS

C_d	drag coefficient
C_{fx}	force coefficient in x-direction
C_{fy}	force coefficient in y-direction
C_ℓ	lift coefficient
J	transformation jacobian
ℓ	body length
P	transformation coordinate control parameter
p	pressure
Q	transformation coordinate control parameter

r	radial variable
r_c	vortex core radius
r_o	vortex core outer radius
Re	Reynolds number, $U_\infty \ell/\nu$
t	time
u	velocity component in the x-direction
v	velocity component in the y-direction
x	Cartesian coordinate
y	Cartesian coordinate
α	coordinate transformation coefficient
β	coordinate transformation coefficient
γ	coordinate transformation coefficient
Γ	circulation
η	coordinate in transformed space
θ	incidence angle
ν	kinematic viscosity
ξ	coordinate in transformed space
ψ	azimuth angle
ω	vorticity

Subscripts

$(\ )_{vw}$	interacting vortex wake quantity, derivative with respect to
$(\ )_o$	reference value
$(\ )_1$	value at body surface

Superscripts

( )' dimensional quantity

INTRODUCTION

The numerical prediction for the strong interaction between vortical wakes and the viscous flow field about bodies is of considerable importance in the design analysis of rotorcraft. The flow field surrounding a helicopter configuration is highly complex because of the lack of symmetry and the unsteady aspects of the flow. This unsteady, asymmetric flow field is complicated further in that the shed wake from the rotor blades interacts with other components of the aircraft (e.g., the rotor blades, fuselage, tail boom, and tail rotor). In general, these are strong interactions in which the rotor wake flows onto or passes very close to the other components of the aircraft. Vortex interactions occur at many flight attitudes (i.e., hover, descent, and low speed flight) and therefore have profound effects on the overall aerodynamic efficiency of the rotorcraft. The effects of the vortex interactions are realized as increased vibratory loading on the fuselage, decreased payload capabilities, and increased noise.

Because of the complexity of the problem and the limitations of the computer in modeling flow field, the research effort addressing vortex interaction for rotorcraft has developed in two directions: blade-vortex interaction and rotor-fuselage interaction. Most of the vortex interaction research for rotorcraft has been directed toward blade-vortex interaction in forward flight. Blade-vortex research has concentrated on the flow field near the rotor tip on the advancing side of the rotor. The flow field in this region is transonic and the rotor blade is at near-zero incidence. Navier-Stokes calculations of blade-vortex interaction are being conducted with increasing efficiency (refs. 1 and 2). These calculations model limited separation because of the incidence of the blade and flow velocity. In addition, the blade-vortex interaction is generally not a direct interaction between the rotor blade and the rotor wake, but a very close passage. The exception is descent in which the rotor wake is convected through the rotor and directly interacts with the rotor blades. The flow beneath the rotor near the fuselage is quite different. Collisions between the rotor wake and the fuselage are present everywhere, the flow is subsonic, and regions of large separation exist.

In contrast to blade-vortex interactions, which occur near the rotor tip, vortex interactions beneath the rotor occur on the entire rotorcraft fuselage. The rotor-fuselage interaction has received far less attention than the blade-vortex interaction. An overview of the rotor-fuselage interactional aerodynamics can be found in reference 3. These interactions, which exist for most flight configurations, are caused by the impingement of the convected rotor wake onto the fuselage components. In contrast to the blade-vortex interaction, the flow field of the rotor-fuselage interaction is subsonic, highly separated, and vortex-dominated. The fuselage is immersed in the rotor downwash, which is an unsteady flow with very large velocity gradients just inboard of the rotor tip. The fuselage is not streamlined in the direction of the downwash; as a consequence, separated wakes form at the surface. These separated wakes are very unsteady because of the interaction of the impinging rotor wake. The result of the vortex interaction is the coupling of the vorticity produced at the surface of the fuselage with the interacting vortex wake. The flow becomes increasingly unsteady owing to the mutual convection between the interacting vortex wake and the surface vorticity. The resulting flow field is very complex, and therefore difficult to model and predict.

The analysis of rotor-fuselage interactions as well as blade-vortex interactions is complicated further by the computational restriction on mesh size. The effects of the mesh size appear in the available computer memory, the computational effort, and the ability of the numerical method to accurately describe the interacting vortex wake over long periods of time. Currently, the available computer memory is inadequate for the three-dimensional mesh necessary to model the flow field surrounding a representative rotorcraft. Therefore, the computational mesh enclosing a body is generally concentrated near the body to resolve the flow at that location and is considerably less dense away from the body. Owing to numerical diffusion, the coarse mesh away from the body is inadequate for accurate predictions of the vortex dynamics surrounding rotorcraft. To calculate the rotor-fuselage interaction, a method is needed to accurately predict both the vortex dynamics away from the body on a coarse mesh and the separated viscous flow near the body surface.

In this paper, a method is presented to calculate the unsteady, two-dimensional, incompressible interaction of a vortex wake with the separated flow about bodies. The method solves the velocity/vorticity formulation of the Navier-Stokes equations. The computational mesh is concentrated near the body surface to resolve the boundary layer and is increasingly coarse further from the body. The interacting vortex wake is modeled as an array of finite-core vortices (refs. 4 and 5). The core radius is variable and is independent of the mesh spacing. The finite-core model eliminates the numerical diffusion associated with the coarse mesh spacing and provides for the accurate prediction of the vortex wake dynamics away from the body, where the flow field is inviscid and dominated by the rotor wake. Closer to the body, the flow is viscous and the convection of the rotor wake can no longer be considered inviscid. In this region the rotor wake interacts with the viscous separated wake and can no longer be represented by a finite-core model. The vortex core is acted upon by shearing forces which will contort and possibly separate the vortex core into several separate vortices. At this point the finite-core vortex is distributed to the computational mesh and allowed to convect as part of the viscous solution.

The solution is started impulsively at $t = 0$. The interacting vortex wake is inserted into the flow field at a selected time and position. This method has been applied to the solution of flow about circular and elliptic cylinders without the presence of an interacting vortex wake and for the interaction of a vortex wake with the flow about an elliptic cylinder at 45° incidence.

Problem Formulation

The vortex interaction problem is modeled by the velocity/vorticity form of the unsteady incompressible Navier-Stokes equations. The governing equations are

for the velocity,

$$\nabla^2 u = -\omega_y \; , \qquad \nabla^2 v = \omega_x \tag{1a,b}$$

and for the vorticity,

$$\omega_t + (u\omega)_x + (v\omega)_y = 1/Re(\nabla^2\omega) \tag{2}$$

with

$$\nabla^2 = \partial(\ )^2/\partial x^2 + \partial(\ )^2/\partial y^2,$$

$$(\ )_t = \partial(\ )/\partial t, \ (\ )_x = \partial(\ )/\partial x, \ (\ )_y = \partial(\ )/\partial y,$$

$$(\ )_{xx} = \partial(\ )^2/\partial x^2 \qquad (\ )_{yy} = \partial^2(\ )/\partial x^2$$

where (x,y) are the Cartesian coordinates, Re is the Reynolds number, and t is the time. The variables (u,v) are the Cartesian components of the velocity and the vorticity ω is defined by

$$\omega = v_x - u_y \tag{3}$$

The nondimensional variables are written

$$x = x'/\ell, \ y = y'/\ell, \ u = u'/U_\infty, \ v = v'/U_\infty$$

$$\omega = \omega'/(U_\infty/\ell), \ t = t'/(\ell/U_\infty), \ Re = U_\infty \ell/\nu$$

where

ℓ = the body length

Re = Reynolds number based on body length

U_∞ = free stream velocity

ν = kinematic viscosity

A body-fitted computational mesh is used in the finite-difference solution to the governing equations. The methodology developed in reference 6 is used for the mesh generation. The method solves for the curvilinear coordinates as solutions of an elliptic differential system. The nomenclature is that of reference 6. The transformed coordinates are solutions of the equations

$$\xi_{xx} + \xi_{yy} = P(\xi,\eta) \tag{4a}$$

$$\eta_{xx} + \eta_{yy} = Q(\xi,\eta) \tag{4b}$$

where (ξ,η) are the transformed coordinates, P and Q are functions used for coordinate control.

In the transformed plane, equations (4a) and (4b) become

$$\alpha x_{\xi\xi} - 2\beta x_{\xi\eta} + \gamma x_{\eta\eta} + J^2(Px_\xi + Qx_\eta) = 0 \tag{5a}$$

$$\alpha y_{\xi\xi} - 2\beta y_{\xi\eta} + \gamma y_{\eta\eta} + J^2(Py_\xi + Qy_\eta) = 0 \tag{5b}$$

The boundary conditions for equations (5a) and (5b) are the specified Cartesian coordinates at the body and the far-field boundary. The computational mesh and transformed coordinates are shown in figure 1.

The governing equations can now be written for the transformed plane. For the velocity components

$$\alpha u_{\xi\xi} - 2\beta u_{\xi\eta} + \gamma u_{\eta\eta} + J^2(Pu_\xi + Qu_\eta) = -J(x_\xi\omega_\eta - x_\eta\omega_\xi) \tag{6a}$$

$$\alpha v_{\xi\xi} - 2\beta v_{\xi\eta} + \gamma v_{\eta\eta} + J^2(Pv_\xi + Qv_\eta) = J(y_\eta\omega_\xi - y_\xi\omega_\eta) \tag{6b}$$

and for the vorticity

$$\begin{aligned}\omega_t &+ [y_\eta(u\omega)_\xi - y_\xi(u\omega)_\eta]/J + [x_\xi(v\omega)_\eta - x_\eta(v\omega)_\xi]/J \\ &= (\alpha\omega_{\xi\xi} - 2\beta\omega_{\xi\eta} + \gamma\omega_{\eta\eta})/(ReJ^2) + (P\omega_\xi + Q\omega_\eta)/Re\end{aligned} \tag{7}$$

where

$$(\ )_t = \partial(\ )/\partial t,\ (\ )_\xi = \partial(\ )/\partial\xi,\ (\ )_\eta = \partial(\ )/\partial\eta,$$

$$(\ )_{\xi\xi} = \partial^2(\ )/\partial\xi^2 \qquad (\ )_{\eta\eta} = \partial^2(\ )/\partial\eta^2$$

$$(\ )_{\xi\eta} = \partial^2(\ )/\partial\xi\partial\eta$$

The boundary conditions for equations (6) and (7) are

$$\begin{aligned}&u = 0,\ v = 0 \text{ at the body surface,}\\ &u = \cos(\theta),\ v = \sin(\theta) \text{ at the far-field boundary}\end{aligned} \tag{8}$$

and

$$\begin{aligned} &\omega = (y_\eta v_\xi + x_\eta u_\xi)/J \quad \text{at the body, and} \\ &\omega = 0 \quad \text{at the far-field boundary} \end{aligned} \tag{9}$$

where θ is the incidence of the body to the free stream flow. The solution is started impulsively at $t = 0$. Instantaneously after the impulsive start, $t = 0+$, the flow is defined by a combination of potential flow and a sheet of vorticity at the body surface.

A third-order-polynomial distribution of vorticity about the vortex position is used to represent the vortex core (ref. 4). This distribution of vorticity is

$$\omega_{vw}(r) = \Gamma/(2\pi r_o^2)[20/3(r^3/r_o^3) - 10(r^2/r_o^2) + 10/3] \tag{10}$$

where ω_{vw} represents the vorticity of the interacting vortex wake and r_o is the outer radius of the vortex distribution. The core radius, the radial position of maximum tangential velocity, is equal to $0.6376\ r_o$. The influence of the interacting vortical wake is included in equations (6a) and (6b) through the x and y components of $-(\bar{\nabla} \times \bar{\omega}_{vw})$. The interacting vortex wake is modeled as an array of finite-core vortices prior to the interaction. However, when the interacting vortex wake is less than a "prescribed" distance from the body surface, the finite-core model is no longer adequate to model the wake. At this point, the interacting vortex wake is distributed to the computational mesh and included as part of the viscous solution.

The surface pressure is obtained by the line integral of the Navier-Stokes equation along the body. At the surface

$$p_\eta = -(\beta\omega_\eta - \alpha\omega_\xi)/(\mathrm{Re}J) \tag{11}$$

or

$$p_1 = p_o - 1/\mathrm{Re} \int_{\eta_o}^{\eta_1} [(\beta\omega_\eta - \alpha\omega_\xi)/J]d\eta \tag{12}$$

where p_1 is the pressure on the surface and p_o is the reference pressure on the surface.

The reference pressure is obtained by the line integral of the Navier-Stokes equation from the far-field boundary to the body surface along a constant η line.

$$p_o = \int_{\xi_1}^{\xi_{max}} [(x_\xi u + y_\xi v)_t - (x_\xi v\omega - y_\xi u\omega) + (\gamma\omega_\eta - \beta\omega_\xi)/(\mathrm{Re}J)]d\xi + 1/2 \tag{13}$$

The force components acting on the body are calculated from the integration of the pressure and shearing forces at the body surface. The force coefficients are

$$C_{fx} = -\int_{\eta_1}^{\eta_2} (p_1 y_\eta) d\eta - (1/Re) \int_{\eta_1}^{\eta_2} (\omega_1 x_\eta) d\eta \tag{14a}$$

$$C_{fy} = \int_{\eta_1}^{\eta_2} (p_1 x_\eta) d\eta - (1/Re) \int_{\eta_1}^{\eta_2} (\omega_1 y_\eta) d\eta \tag{14b}$$

where ω_1 is the vorticity at the body.

The lift and drag coefficients are

$$C_\ell = -C_{fx}[\sin(\theta)] + C_{fy}[\cos(\theta)] \tag{15a}$$

$$C_d = C_{fx}[\cos(\theta)] + C_{fy}[\sin(\theta)] \tag{15b}$$

where θ is the incidence of the body with respect to the free-stream flow.

Numerical Method

The governing equations are solved by standard finite-difference methods on the body-fitted computational mesh. The mesh is concentrated near the body to resolve the flow at that location.

The vorticity transport equation, equation (7), is solved using an alternating direction implicit method (ADI) (ref. 7). The ADI method solves the time-dependent vorticity transport equation by separating the equation into two implicit equations for a single time-step.

The finite difference expression for the vorticity transport equation is

$$(\omega^{n+1/2} - \omega^n)/(\Delta t/2) + [y_\eta (u\omega)_\xi^{n+1/2} - y_\xi (u\omega)_\eta^n]/J + [x_\xi (v\omega)_\eta^n - x_\eta (v\omega)_\xi^{n+1/2}]/J$$

$$= (\alpha\omega_{\xi\xi}^{n+1/2} - 2\beta\omega_{\xi\eta}^n + \gamma\omega_{\eta\eta}^n)/(ReJ^2) + (P\omega_\xi^{n+1/2} + Q\omega_\eta^n)/Re \tag{16a}$$

for the ξ-derivatives, and

$$(\omega^{n+1} - \omega^{n+1/2})/(\Delta t/2) + [y_\eta (u\omega)_\xi^{n+1/2}$$

$$- y_\xi (u\omega)_\eta^{n+1}]/J + [x_\xi (v\omega)_\eta^{n+1} - x_\eta (v\omega)_\xi^{n+1/2}]/J$$

$$= (\alpha\omega_{\xi\xi}^{n+1/2} - 2\beta\omega_{\xi\eta}^{n+1/2} + \gamma\omega_{\eta\eta}^{n+1})/(ReJ^2) + (P\omega_\xi^{n+1/2} + Q\omega_\eta^{n+1})/Re \tag{16b}$$

for the η-derivatives.

The vorticity at the body surface in equation (16b) is calculated from equation (9) whereas the vorticity at the body surface at the half time-step is calculated from equations (16a) and (16b) as

$$\omega^{n+1/2} = (1/2)(\omega^{n} + \omega^{n+1}) + \Delta t/(4ReJ^{2})[(\gamma\omega^{n}_{\eta\eta} - \gamma\omega^{n+1}_{\eta\eta})] + (\Delta tQ)/(4Re)[\omega^{n}_{\eta} - \omega^{n+1}_{\eta}] \qquad (17)$$

The convective velocity at the half time-step in equations (16a) and (16b) is calculated from the average of the n and $n + 1$ values of the velocity.

The velocity equations (6a) and (6b) are cast in a time-dependent form and solved by the ADI method.

The influence of the interacting vortex wake is included in the velocity equations through the negative curl of the vorticity distribution in the vortex core, $-(\bar{\nabla} \times \bar{\omega}_{vw})$. The vorticity distribution in the vortex core is defined in equation (10). Outside the outer radius, the vorticity is zero.

The solution to the time-dependent problem is calculated by solving the vorticity transport equation, updating the interacting-vortex-wake position, and then solving the velocity equations.

Computed Results

Results for the viscous flow about two-dimensional bodies have been calculated with and without an interacting vortex wake. The flow around circular and elliptic cylinders in the absence of an interacting vortex wake has been calculated in order to compare results of the current method with those of other numerical studies and experimental investigations. The flow around the circular cylinder was calculated for a Reynolds number of 3000. The flow around the elliptic cylinder was calculated for Reynolds numbers 200 and 3000 at 45° incidence.

The interaction of a vortex wake with the flow around an elliptic cylinder at 45° incidence and a Reynolds number of 3000 was calculated. The interacting vortex wake models the periodic passage of a vortex generated by a rotor blade.

No Vortex Interaction Case

Circular Cylinder- The flow about a circular cylinder was calculated at a Reynolds number of 3000. This condition was selected because there exists data at this Reynolds number for comparison. In addition, the emergence of several secondary vortices behind the cylinder has been calculated numerically and observed experimentally. The computational mesh is 81×241 with the far field boundary at 20 radii. The variation of the drag coefficient with time is shown in figure 2. The time, $t = 1.0$, corresponds to the time required to travel a distance equal to the cylinder radius at a velocity equal to that of the free-stream velocity. The effect of the secondary vortices on the drag coefficient can be seen as the small variations in the curve. The distribution of the boundary vorticity at the cylinder surface is shown in figure 3. These results are in excellent agreement with the results of the numerical investigation of reference 8. The distribution of the u-component of velocity along the x-axis behind the cylinder is shown in figure 4. Experimental results from reference 9 and the numerical results of reference 8 are included in the figure for comparison. The comparison in the data is shown to be quite good. The streamline contours for the developing flow around the circular cylinder are shown in figure 5. The flow patterns demonstrate the emergence of the secondary vortices and are similar to those reported in references 8 and 9.

Elliptic cylinder- The flow around an elliptic cylinder at 45° incidence was calculated at Reynolds numbers of 200 and 3000. The computational mesh is 41×161 for Reynolds number 200 and 81×241 for Reynolds number 3000. The far-field boundary is equivalent to 20 radii. The time evolution of the lift and drag coefficients is shown in figure 6 for Reynolds number 200. The time, $t = 1.0$, corresponds to the time required to travel a distance equal to the elliptic cylinder semi-major axis at a velocity equal to that of the free-stream velocity. The results compare favorably with the results of reference 10 up to $t = 8$. The exact trend in the data of reference 10 for $t > 9.0$ is unclear because those data were limited. The development in time of the streamlines around the elliptic cylinder are shown in figure 7 for a Reynolds number of 200. The streamline contours are similar to those reported in reference 10.

Variations in the lift and drag coefficients with time for the flow around an elliptic cylinder at Reynolds number 3000 are shown in figure 8. The cylinder is again at 45° incidence. The loading on the elliptic cylinder is shown to be more dynamic than that of the circular cylinder (see fig. 2). This is due to the large velocity gradient and resulting surface vorticity at the leading edge of the elliptic cylinder. In addition, the secondary vortex structure near the leading edge on the upper surface of the cylinder contributes significantly to the dynamic loading on the cylinder. The development in time of the streamlines around the cylinder are presented in figure 9. The development of the secondary vortices can be clearly seen. The separated wake behind the cylinder is shown to be very dynamic due to the strength and periodic shedding of vortices from the leading and trailing edges of the cylinder.

Vortex Interaction Case

The interaction of a vortex wake with the flow about an elliptic cylinder at 45° incidence and a Reynolds number of 3000 was calculated. The computational mesh is 81×241 with the far field boundary at 20 radii. Two interactions were considered, the difference between the interactions being the sign of the interacting vortex wake. Each interaction modeled the interacting vortex wake as an array of vortices inserted into the flow field at constant time intervals. This represents the periodic passage of a rotor blade and the associated tip vortex, thus generating the rotor's vortical wake structure. The orientation of the interacting vortex wake with respect to the elliptic cylinder is depicted in figure 10. In each interaction the vortices are of constant strength and equal to $\Gamma = -1.0$ for the first interaction and $\Gamma = 1.0$ for the second interaction. For both interactions $r_o = 0.1$. The flow was started impulsively at $t = 0$. Five equally spaced vortices are inserted into the flow field forward of the elliptic cylinder at $t = 0.25$. The flow around the elliptic cylinder is very unsteady; therefore, an optimum time to insert the vortices into the flow was not obvious. The time, $t = 0.25$, was chosen to minimize the effects of the impulsive start. A new vortex is inserted at a constant time interval, $t = 1.0$, during the remainder of the solution. A vortex is distributed to the mesh when the distance between the vortex position and the surface of the elliptic cylinder is less than 0.75.

First Interaction, $\Gamma = -1.0$- The lift and drag variations with time are shown in figures 11(a) and 11(b), respectively. Also shown on each figure is the respective value of the lift and drag coefficient for the elliptic cylinder in the absence of the interacting vortex wake. Initially, for $t < 0.25$, the lift and drag coefficients are identical to those calculated for the elliptic cylinder without the interacting vortex wake. However, after the interacting vortex wake is inserted into the flow, $t = 0.25$, the loading on the cylinder changes drastically.

These changes seem to occur at $t = 0.5$ with a gradual decrease in the lift, figure 11(a), and drag, figure 11(b). At this time, the interacting vortex wake is below the cylinder and does not significantly affect the flow near the cylinder which is dominated by vortices generated by the cylinder during the impulsive start. As the interaction proceeds for $t = 1.0$, the lift (fig. 11(a)) and the drag (fig. 11(b)) are significantly reduced from those in the absence of the interacting vortex wake. The signature of individual vortices comprising the interacting vortex wake can be seen as spikes in the development of the lift coefficient (fig. 11(a)) at times $t = 2.0$, 3.0, 5.0, 7.0, and 8.5. Similar spikes can be seen in the development of the drag coefficient (fig. 11(b)) although less pronounced.

The streamlines during the interaction are shown in figure 12. Initially, figure 12(a), the flow field is similar to that in the absence of the interacting vortex wake (fig. 9(a)) with the exception that the incoming streamlines have been rotated clockwise and the forward stagnation point has moved toward the leading edge. These flow changes are caused by the induced velocity of the interacting vortex wake and result in a reduction in the effective angle of attack of the elliptic cylinder. A reduction in the angle of attack decreases the strength of the separated vortices at the leading edge of the cylinder and changes the position of the secondary vortices. The secondary vortex structure is positioned farther downstream of the leading edge (figs. 12(b-d)) when compared to the flow with no vortex interaction (figs. 9(b-d)).

At later times (figs. 12(f-i)), the significant aspect of the flow is the generation of a strong vortex at the trailing edge of the cylinder. This vortex is caused by the increased flow around the trailing edge from lower to upper surface due to the interacting vortex wake and results in a very dynamic separated wake behind the cylinder.

Second interaction, $\Gamma = 1.0$- The lift and drag variations with time shown in figures 13(a) and 13(b), respectively. Here again, the respective value of the lift and drag coefficient for the elliptic cylinder in the absence of the interacting vortex wake are shown for comparison. Initially, for $t < 0.25$ the loading on the cylinder is identical to that for the elliptic cylinder without the interacting vortex wake. Initial changes in the loading on the cylinder during the interaction from that with no vortex interaction occur at $t = 0.5$.

These changes begin with a rapid increase in the lift (fig. 13(a)) and drag (fig. 13(b)). At this time, the interacting vortex wake is upstream of the cylinder. However, the induced velocity caused by the interacting vortices generates an upwash at the leading edge of the cylinder. This upwash increases the relative angle of attack of the cylinder, and therefore the lift and drag on the cylinder. As the interacting vortex wake approaches the cylinder ($t = 1.0$) the lift (fig. 13(a)) and the drag (fig. 13(b)) are significantly increased from those in the absence of the interacting vortex wake. The signature of individual vortices comprising the interacting vortex wake can be seen as spikes in the development of the lift coefficient (fig. 13(a)) at times $t = 1.5$, 2.5, 3.5, 4.8, 6.5, 7.6, and 9.6. Similar spikes can be seen in the development of the drag coefficient (fig. 13(b)).

The streamlines produced during the interaction are shown in figure 14. Initially (fig. 14(a)), the flow field is similar to that in the absence of the interacting vortex wake (fig. 9(a)) and of the previous interaction (fig. 12(a)); however, the incoming streamlines have been rotated counterclockwise thus increasing the effective angle of attack of the cylinder. The increased angle of attack moves the forward stagnation point toward the midchord position and increases the flow around the leading edge of the cylinder. The increased flow at the leading edge of the cylinder increases the strength of the separated vortices generated at that position. In addition, the secondary vortex structure is positioned nearer the leading edge of the cylinder (figs. 14(b-d)) when compared to the flow with no vortex interaction (figs. 9(b-d)) and to the flow of the previous interaction (figs. 12(b-d)).

As the interaction proceeds (figs. 14(f-i)), the generation of the separated vortices at the leading edge of the cylinder dominates the flow.

CONCLUSIONS

A method has been developed to model the two-dimensional interaction between an interacting vortex wake represented by a finite-core model and the viscous flow around arbitrary bodies. The method solves for the flow field velocities on a body-fitted computational mesh using finite-difference techniques. The viscous flow field of the two-dimensional body is calculated on an Eulerian grid via the velocity/vorticity formulation of the Navier-Stokes equations.

A simulation of a rotor wake interaction with the flow about a 4:1 elliptic cylinder at 45° incidence was shown for Reynolds number 3000. The simulation demonstrates the significant variations in the lift and drag on the elliptic cylinder in the presence of the interacting rotor wake. The interacting vortex wake significantly changes the effective incidence of the elliptic cylinder, thereby altering the loading on the elliptic cylinder and the generation of vorticity at the surface of the cylinder.

When the strength of the interacting vortex wake was less than zero (producing a clockwise rotating vortex), the effective incidence of the cylinder (and therefore the loading) was significantly reduced from that for the flow around the cylinder in the absence of the interacting vortex wake. An interacting vortex wake of strength greater than zero had the opposite effect on the flow around the cylinder. The incidence of the cylinder and the loading on the cylinder were greatly increased.

During both interactions, several secondary vortices were generated just aft of the leading edge on the upper surface of the cylinder. Oscillations in the loading on the elliptic cylinder during both interactions were shown. These oscillations were not present in the calculations of the flow in the absence of the interacting vortex wake and are felt to be the result of the increased shedding of secondary vortices.

REFERENCES

1. Srinivasan, G. R.; McCroskey, W. J.; and Baeder, J. D.: Aerodynamics of Two-Dimensional Blade-Vortex Interaction. AIAA Journal, vol. 24, no. 10, Oct. 1986, pp.1569-1576.

2. Rai, M. M.: Navier-Stokes Simulations of Blade-Vortex Interaction Using High-Order Accurate Upwind Schemes. AIAA Paper 87-0543, Reno, NV, 1987.

3. Sheridan, P. F.; and Smith, R. P.: Interactional Aerodynamics - A New Challenge for Helicopter Technology, 35th Annual National Forum of the American Helicopter Society, Washington, DC, May 1979.

4. Stremel, P. M.: A Method for Modeling Finite Core Vortices in Wake Flow Calculations. AIAA Paper 84-0417, Reno, NV, 1984.

5. Stremel, P. M.: Aerodynamic Interaction Between Vortical Wakes and the Viscous Flow about a Circular Cylinder. AIAA Paper 85-4063, Colorado Springs, CO, 1985.

6. Thompson, J. F.; Thames, F. C.; and Mastin, C. W.: Boundary-Fitted Curvilinear Coordinate Systems for Solution of Partial Differential Equations on Fields Containing any Number of Arbitrary Two-Dimensional Bodies. NASA CR-2729, 1977.

7. Peaceman, D. W.; and Rachford, H. H., Jr.: The Numerical Solution of Parabolic and Elliptic Differential Equations, Journal of the Society for Industrial Applied Mathematics, vol. 3, no. 1, 1955, pp. 28-41.

8. Loc, Ta Phuoc; and Bouard, R.: Numerical Solution of the Early Stage of the Unsteady Viscous Flow around a Circular Cylinder: A Comparison with Experimental Visualization and Measurements. J. Fluid Mechanics, vol. 160, 1985, pp. 93-117.

9. Bouard, R.; and Coutanceau, M.: The Early Stage of Development of the Wake behind an Impulsively Started Cylinder for $40 < Re < 10^4$, J. Fluid Mechanics, vol. 101, 1980, p. 583.

10. Lugt, H. J.; and Haussling, H. J.: Laminar Flow past an Abruptly Accelerated Elliptic Cylinder at 45° Incidence. J. Fluid Mechanics, vol. 65, 1974, pp. 711-734.

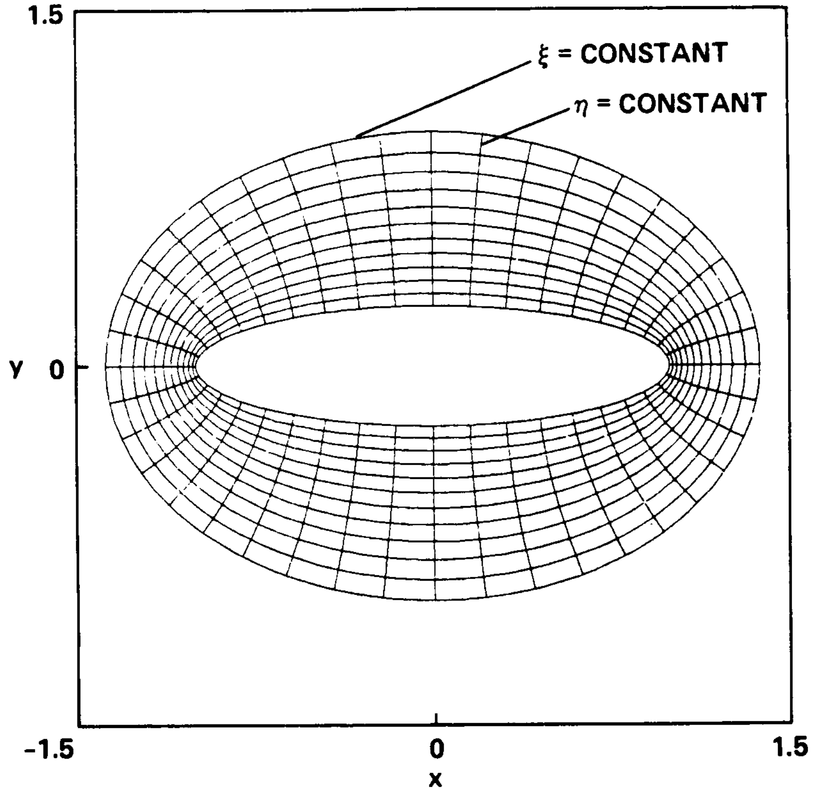

Figure 1.- Computational geometry.

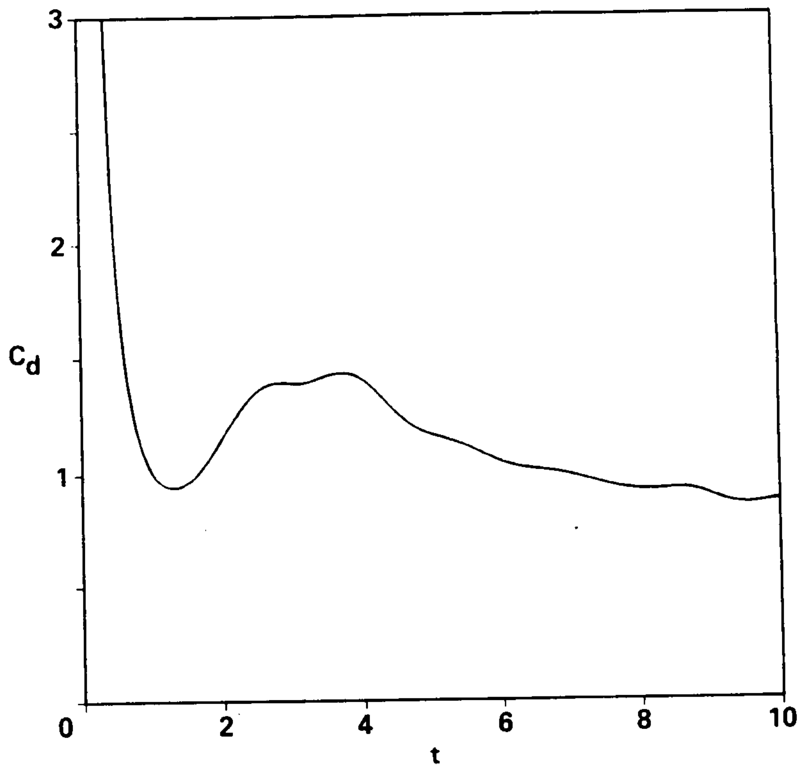

Figure 2.- Drag coefficient, circular cylinder, Re = 3000.

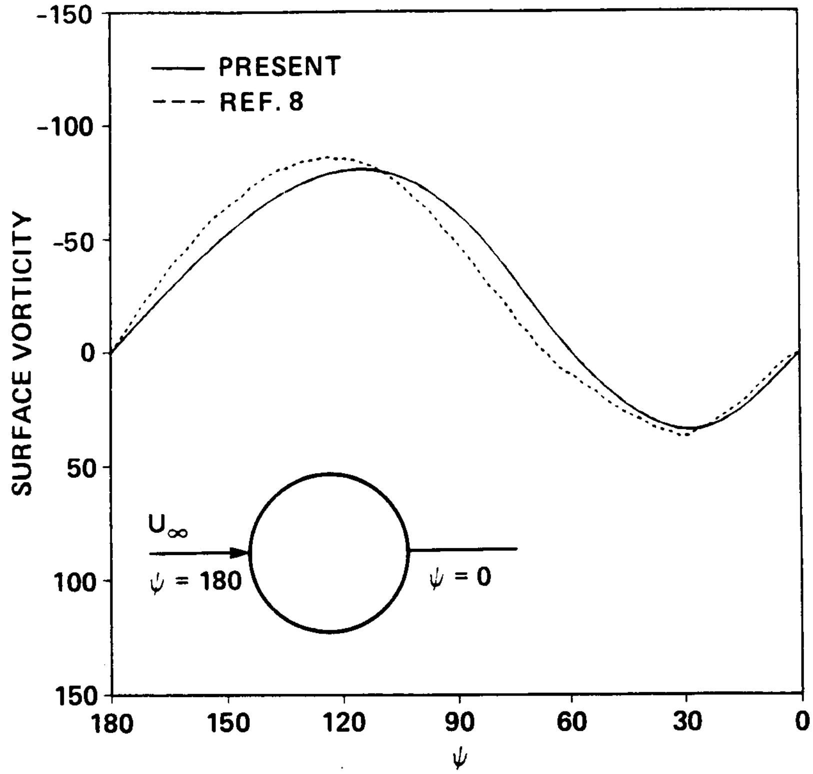

(a) t = 1.00

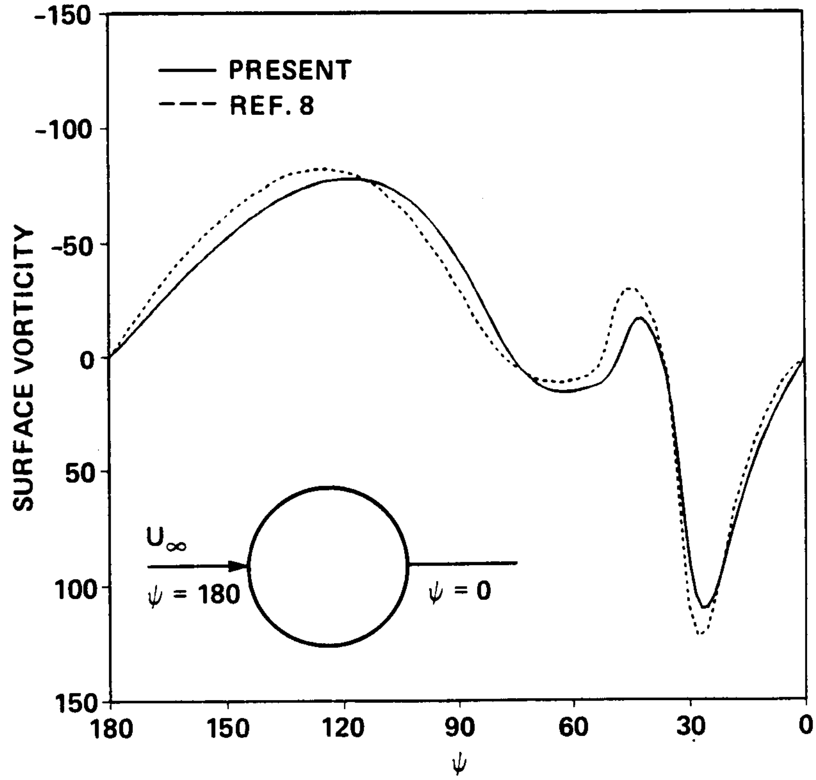

(b) t = 2.00

Figure 3.- Distribution of boundary vorticity at cylinder surface, circular cylinder, Re = 3000.

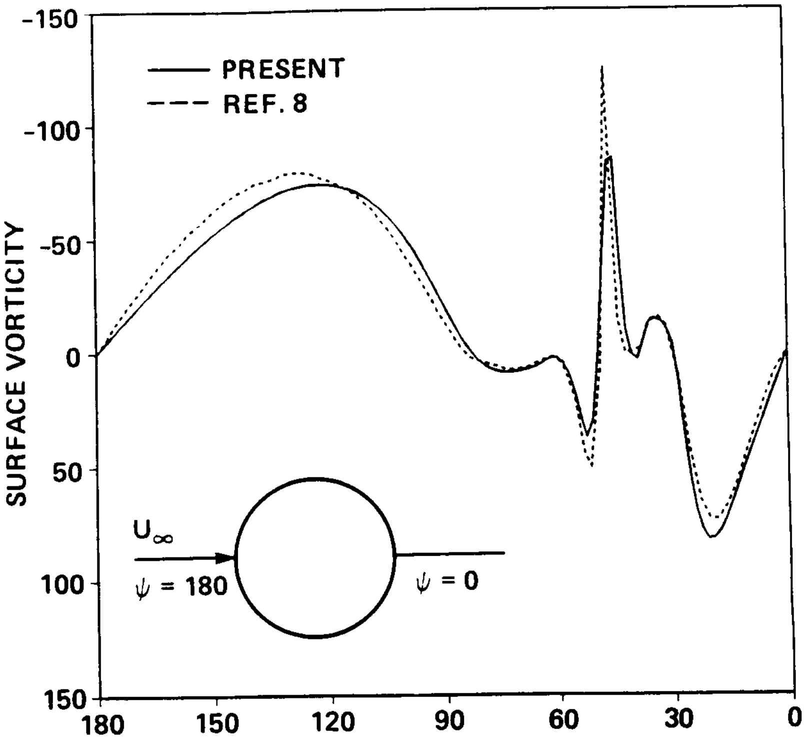

(c) t = 3.00

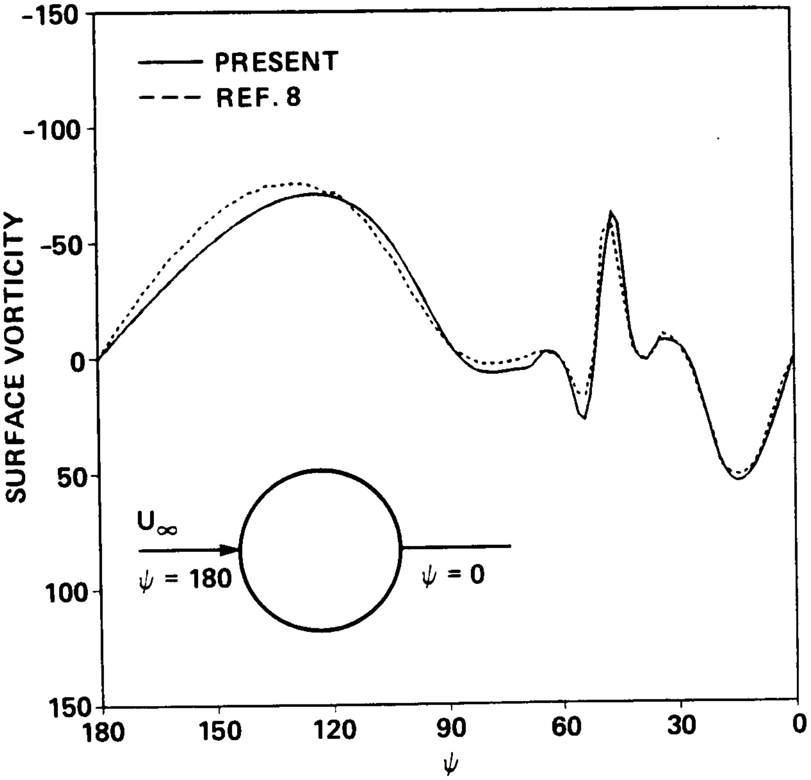

(d) t = 4.00

Figure 3.- Continued.

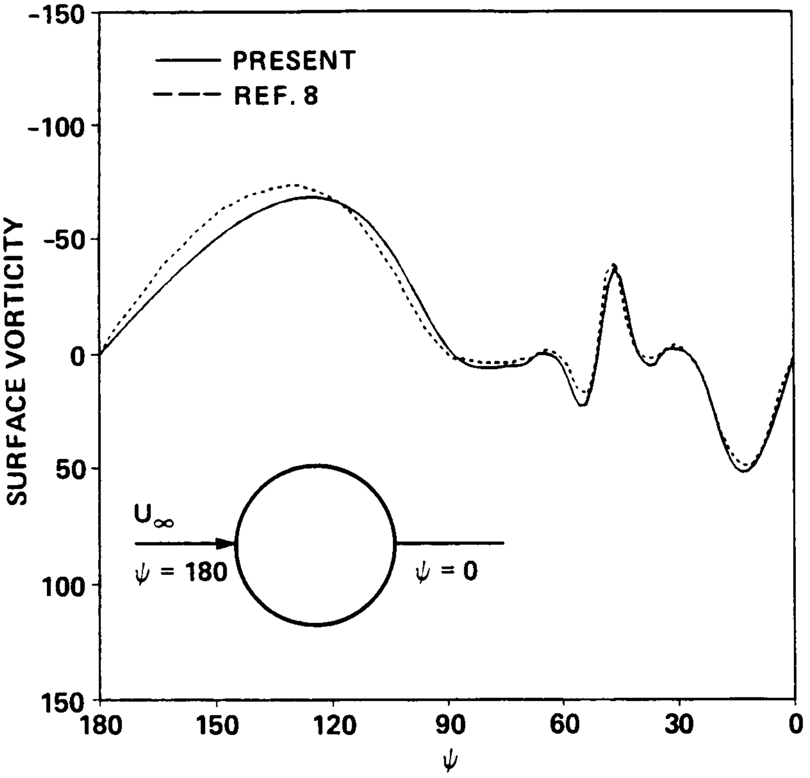

(e) t = 5.00

Figure 3.- Concluded.

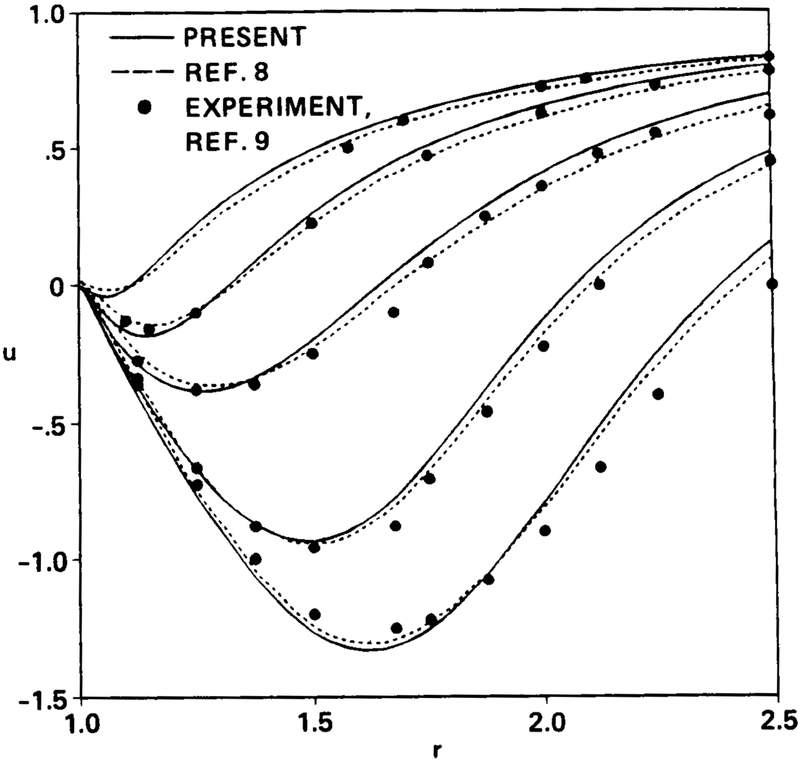

Figure 4.- Velocity profile downstream of circular cylinder, comparison with experiment, u velocity component, Re = 3000.

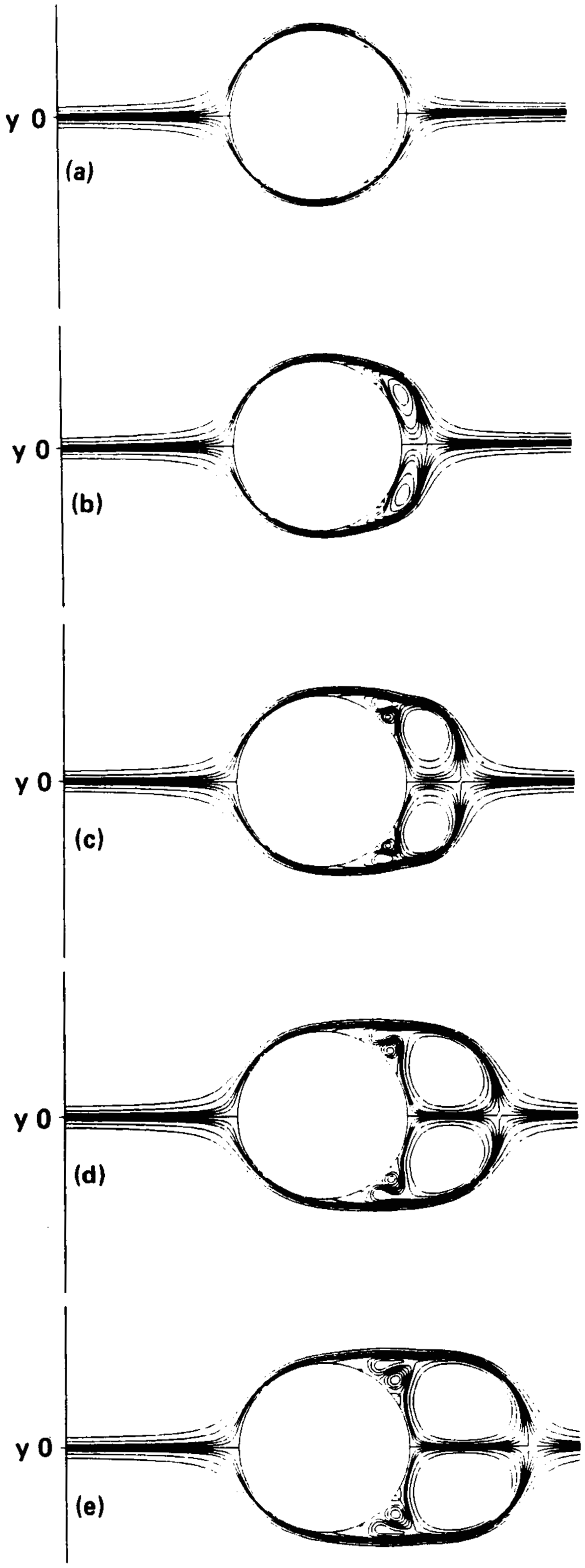

Figure 5.- Streamline contours for circular cylinder, Re = 3000, (a) t = 1.00, (b) t = 2.00, (c) t = 3.00, (d) t = 4.00, and (e) t = 5.00.

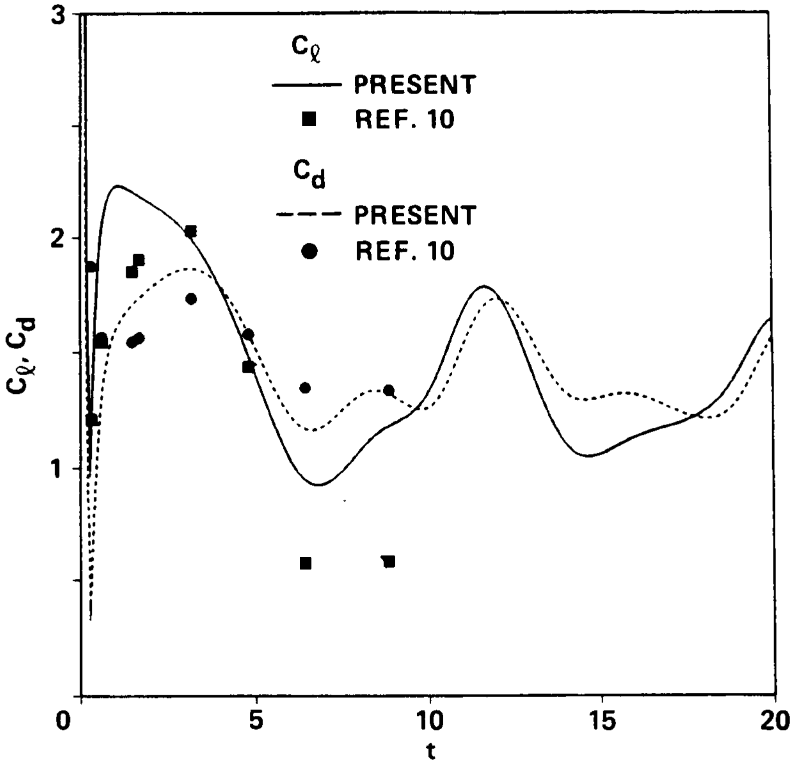

Figure 6.- Lift and drag coefficients, elliptic cylinder, Re = 200, θ = 45°.

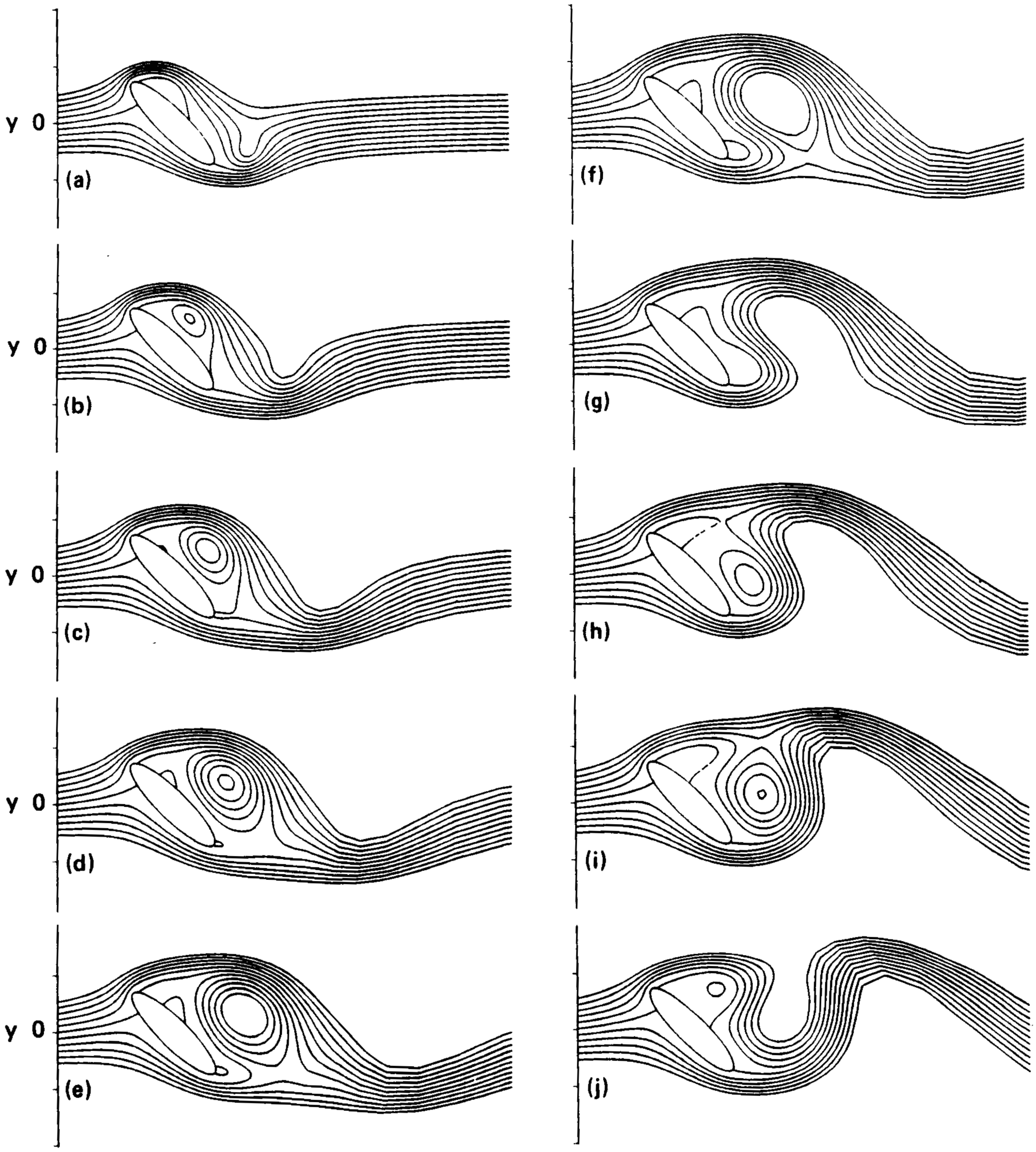

Figure 7.- Streamline contours, elliptic cylinder, Re = 200, θ = 45°. (a) t = 1.00, (b) t = 2.00, (c) t = 3.00, (d) t = 4.00, (e) t = 5.00, (f) t = 6.00, (g) t = 7.00, (h) t = 8.00, (i) t = 9.00, and (j) t = 10.00,

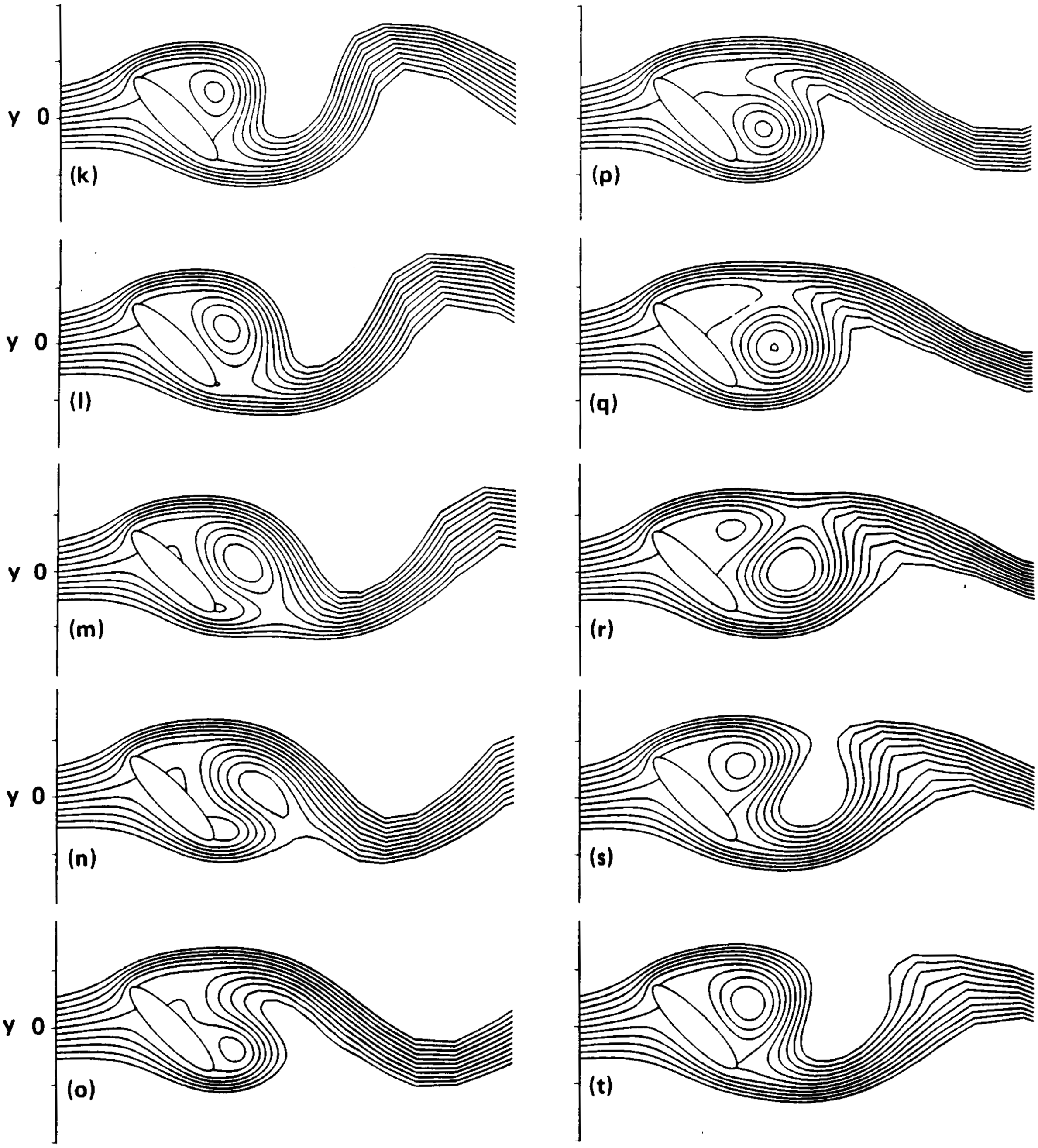

Figure 7.- Concluded. (k) t = 11.00, (l) t = 12.00, (m) t = 13.00, (n) t = 14.00, (o) t = 15.00, (p) t = 16.00, (q) t = 17.00, (r) t = 18.00, (s) t =19.00, and (t) t = 20.00.

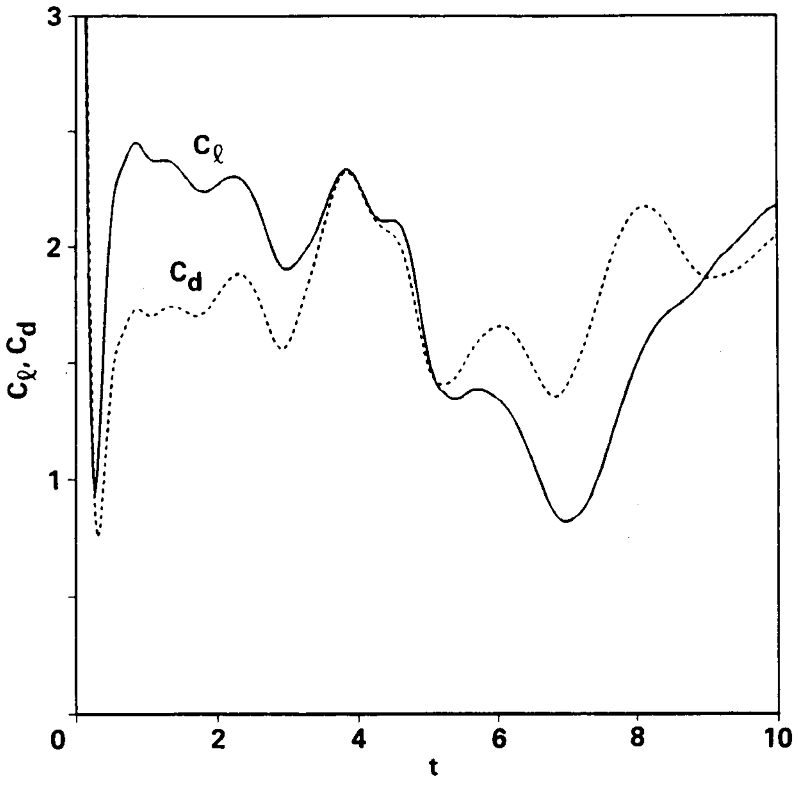

Figure 8.- Lift and drag coefficients, elliptic cylinder, Re = 3000, θ = 45°.

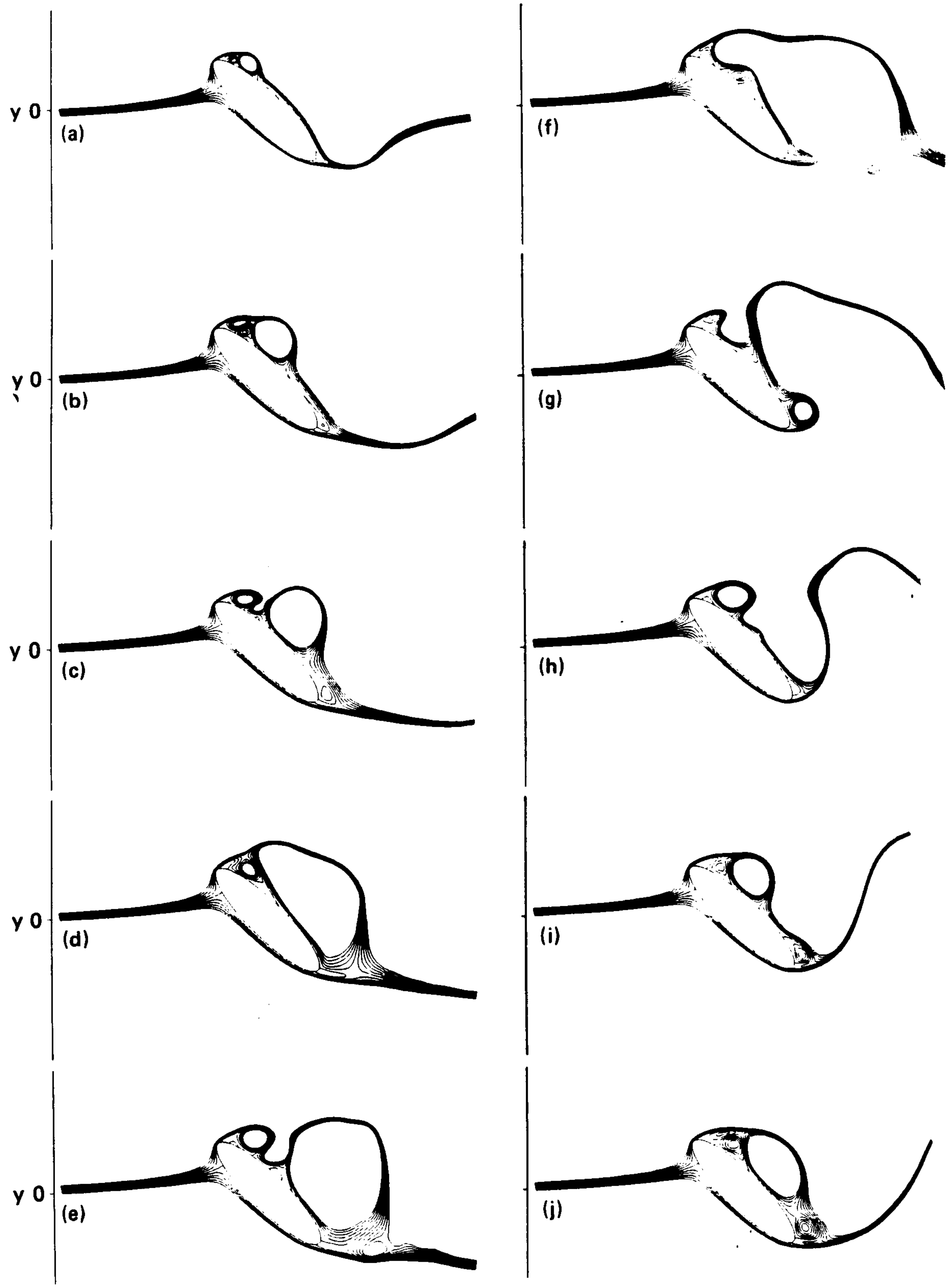

Figure 9.- Streamline contours, elliptic cylinder, Re = 3000, θ = 45°.
(a) t = 1.00, (b) t = 2.00, (c) t = 3.00, (d) t = 4.00, (e) t = 5.00,
(f) t = 6.00, (g) t = 7.00, (h) t = 8.00, (i) t = 9.00, and (j) t = 10.00.

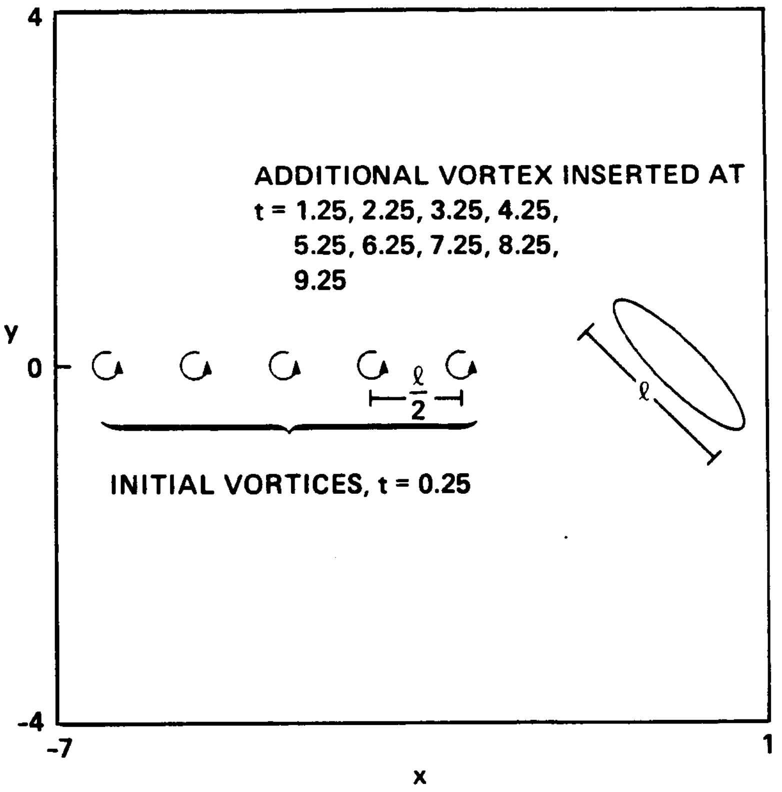

Figure 10.- Schematic of vortex interaction.

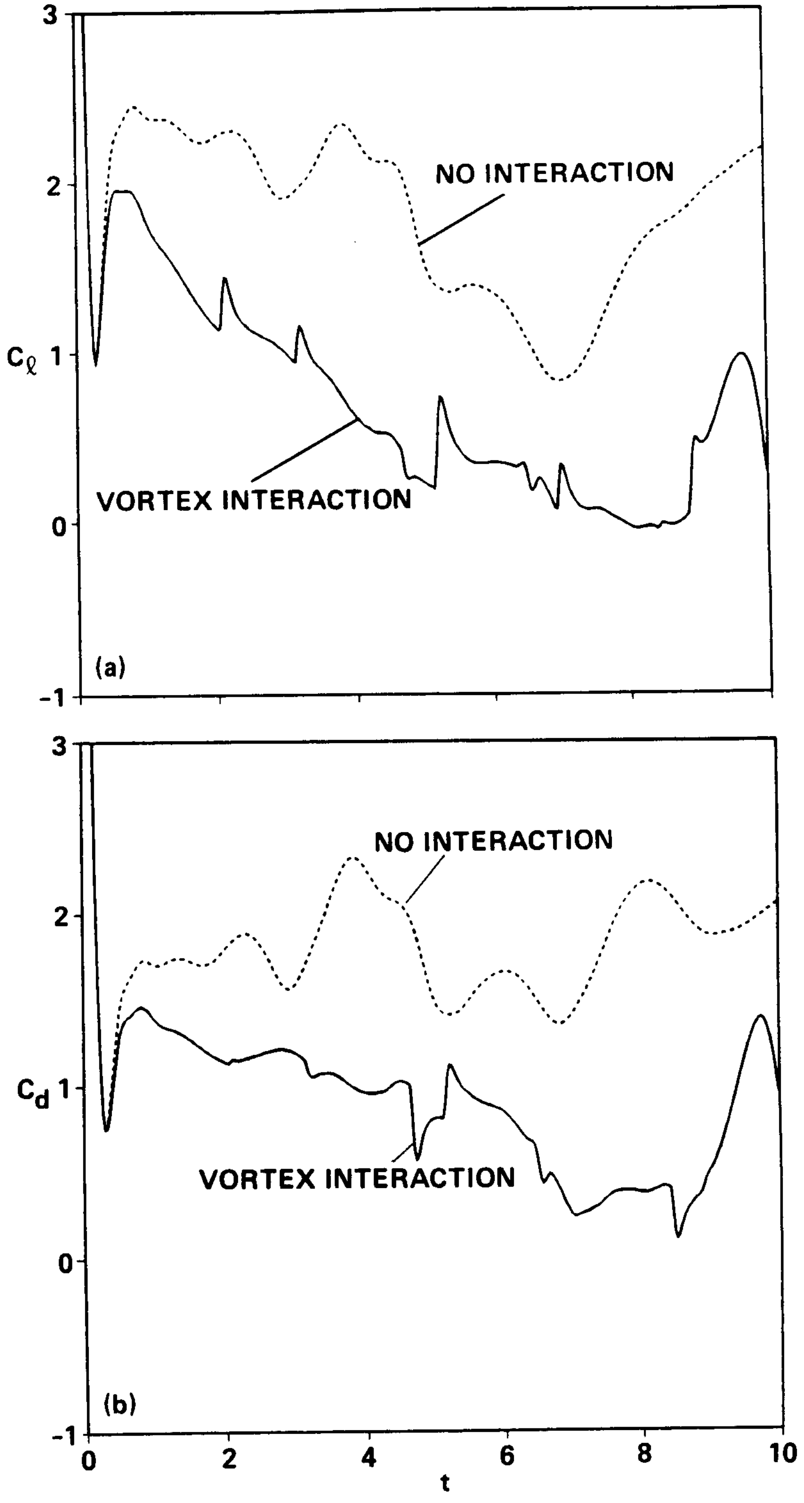

Figure 11.- Vortex interaction, vortex strength $\Gamma = -1.0$, $r_o = 0.1$, elliptic cylinder, Re = 3000, $\theta = 45°$. (a) Lift coefficient; and (b) drag coefficient.

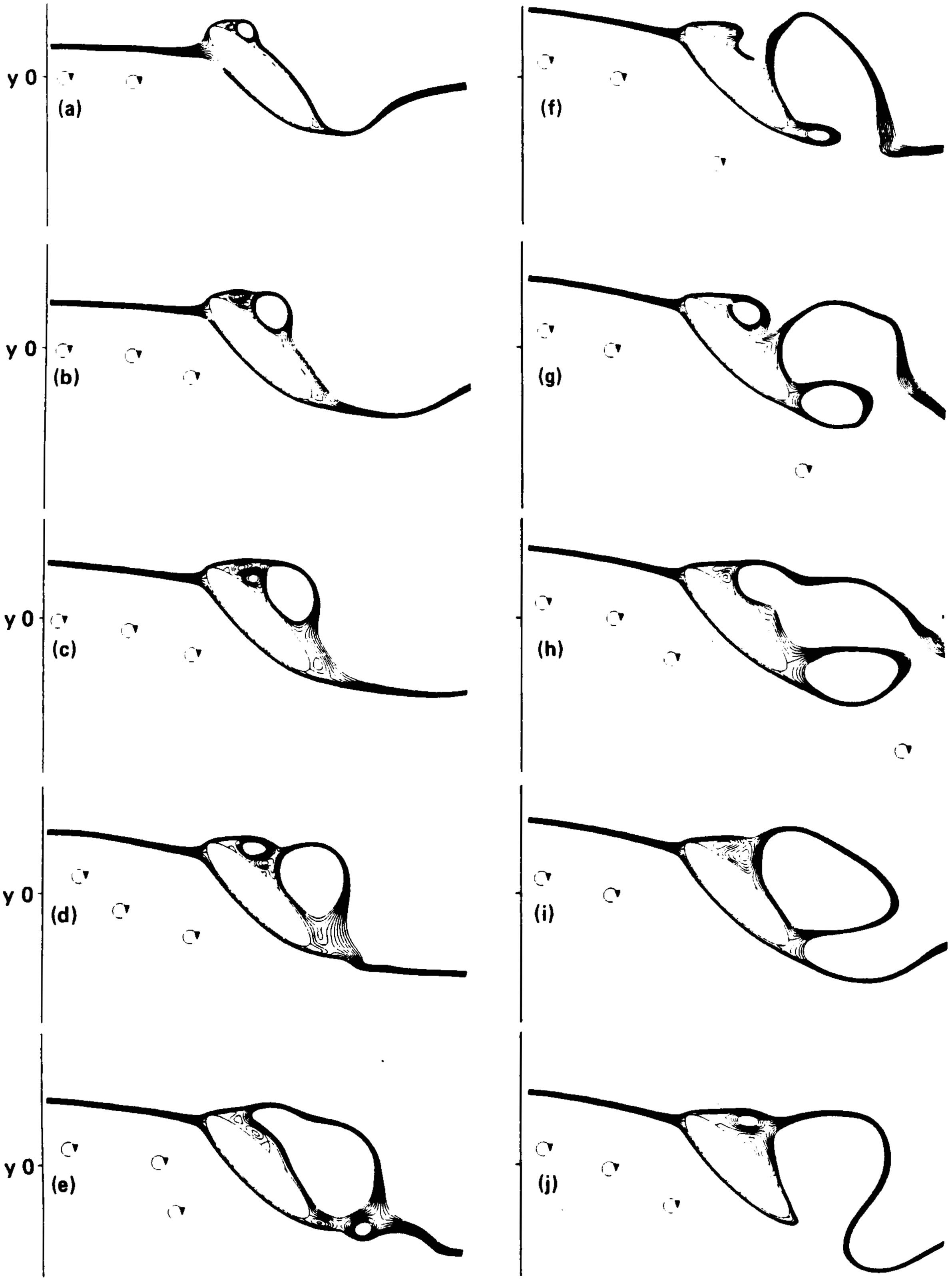

Figure 12.- Streamline contours for a vortex interaction, vortex strength $\Gamma = 1.0$, $r_o = 0.1$, elliptic cylinder, Re = 3000, $\theta = 45°$. (a) t = 1.00; (b) t = 2.00; (c) t = 3.00; (d) t = 4.00; (e) t = 5.00, (f) t = 6.00, (g) t = 7.00, (h) t = 8.00, (i) t = 9.00, and (j) t = 10.00.

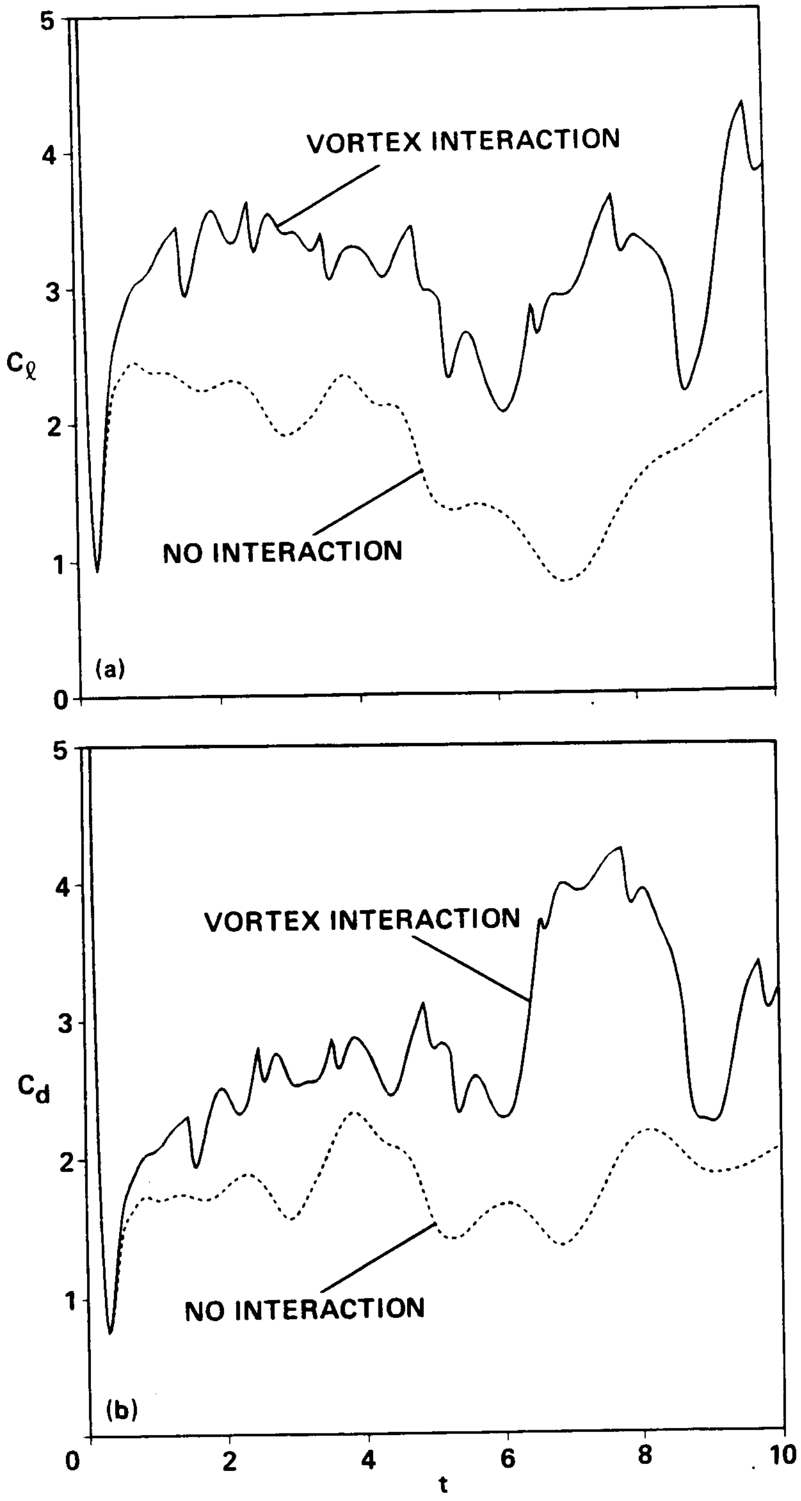

Figure 13.- Vortex interaction, vortex strength $\Gamma = 1.0$, $r_0 = 0.1$, elliptic cylinder, Re = 3000, $\theta = 45°$. (a) Lift coefficient; and (b) drag coefficient.

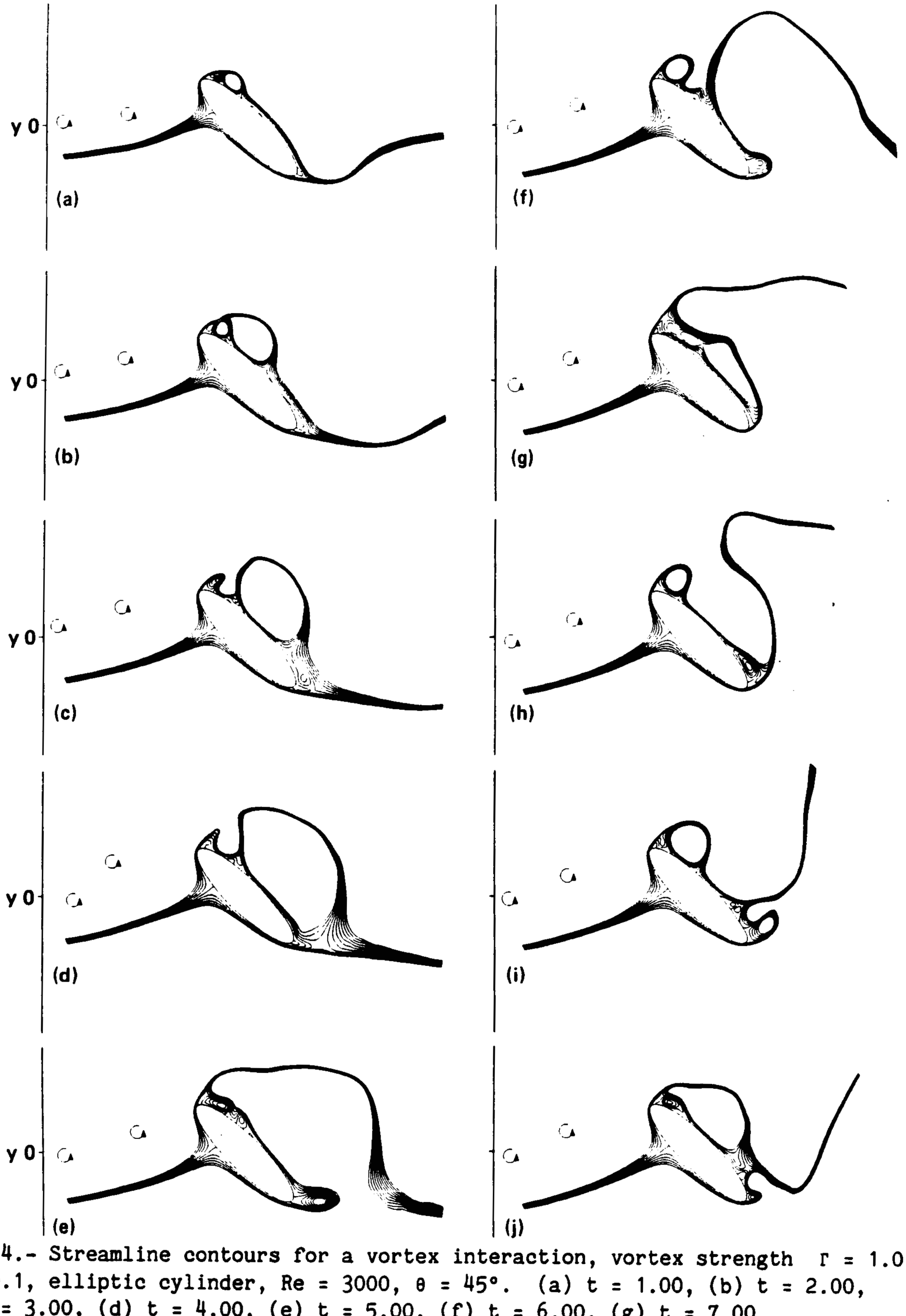

Figure 14.- Streamline contours for a vortex interaction, vortex strength $\Gamma = 1.0$, $r_o = 0.1$, elliptic cylinder, Re = 3000, $\theta = 45°$. (a) t = 1.00, (b) t = 2.00, (c) t = 3.00, (d) t = 4.00, (e) t = 5.00, (f) t = 6.00, (g) t = 7.00, (h) t = 8.00, (i) t = 9.00, and (j) t = 10.00,

National Aeronautics and Space Administration

Report Documentation Page

1. Report No. NASA TM-101074	**2. Government Accession No.**	**3. Recipient's Catalog No.**

4. Title and Subtitle

Aerodynamic Interaction Between Vortical Wakes and Lifting Two-Dimensional Bodies

5. Report Date

March 1989

6. Performing Organization Code

7. Author(s)

Paul M. Stremel

8. Performing Organization Report No.

A-89047

10. Work Unit No.

505-61-51

9. Performing Organization Name and Address

Ames Research Center
Moffett Field, CA 94035

11. Contract or Grant No.

12. Sponsoring Agency Name and Address

National Aeronautics and Space Administration
Washington, DC 20546-0001

13. Type of Report and Period Covered

Technical Memorandum

14. Sponsoring Agency Code

15. Supplementary Notes

Point of Contact: Paul M. Stremel, Ames Research Center, MS TR-31, Moffett Field, CA 94035
(415) 694-6653 or FTS 464-6653

16. Abstract

Unsteady rotor wake interactions with the empennage, tail boom, and other aerodynamic surfaces of a helicopter have a significant influence on its aerodynamic performance, the ride quality, and vibration. A numerical method for computing the aerodynamic interaction between an interacting vortex wake and the viscous flow about arbitrary two-dimensional bodies has been developed to address this helicopter problem. The method solves for the flow field velocities on a body-fitted computational mesh using finite-difference techniques. The interacting vortex wake is represented by an array of discrete vortices which, in turn, are represented by a finite-core model. The evolution of the interacting vortex wake is calculated by Lagrangian techniques. The viscous flow field of the two-dimensional body is calculated on an Eulerian grid. The flow around circular and elliptic cylinders in the absence of an interacting vortex wake has been calculated. These results compare very well with other numerical results and with results obtained from experiment and thereby demonstrate the accuracy of the viscous solution. The interaction of a rotor wake with the flow about a 4:1 elliptic cylinder at 45° incidence was calculated for a Reynolds number of 3000. The results demonstrate the significant variations in the lift and drag on the elliptic cylinder in the presence of the interacting rotor wake.

17. Key Words (Suggested by Author(s)) Unsteady viscous flow, Vortex interaction Velocity/vorticity formulation, Finite-core vortex Circular cylinder, Elliptic cylinder	**18. Distribution Statement** Unclassified-Unlimited Subject Category - 34

19. Security Classif. (of this report) Unclassified	**20. Security Classif. (of this page)** Unclassified	**21. No. of pages** 33	**22. Price** A03

NASA FORM 1626 OCT 86

For sale by the National Technical Information Service, Springfield, Virginia 22161